UJEAS

UNIZIK JOURNAL OF ENGINEERING AND APPLIED SCIENCES

UNIZIK Journal of Engineering and Applied Sciences 6(5), December (2026), 4186-4206
Journal homepage: https://journals.unizik.edu.ng/index.php/ujeas
PRINT ISSN: 2992-4383 || ONLINE ISSN: 2992-4391

# Multifunctional Ni–Cr Modified Ogbunike Clay Catalysts for One-Pot Production of Jet Fuel-Range Hydrocarbons from Calabash Seed Oil

Calista Chimelogo Ejiofor*, Joseph Tagbo Nwabanne, Philomena Kanwulia Igbokwe
Department of Chemical Engineering, Nnamdi Azikiwe University, Awka
*Corresponding Author's E-mail: cc.ejiofor@unizik.edu.ng

**Abstract**
This study investigated the synthesis, physicochemical characterization, and catalytic performance of acid- and alkaline-modified Ogbunike clay and their Ni–Cr-impregnated derivatives for the one-pot upgrading of calabash seed oil to hydrocarbon fuels. Acid-treated clay (ATC) and alkaline-treated clay (BTC) were prepared through acid and alkaline activation, respectively, followed by wet impregnation of nickel and chromium at a Ni:Cr precursor ratio of 2:1. The resulting catalysts were characterized using X-ray fluorescence (XRF), X-ray diffraction (XRD), Fourier-transform infrared spectroscopy (FTIR), Brunauer–Emmett–Teller (BET) surface-area analysis, and density functional theory (DFT) pore-volume analysis. Catalytic performance was evaluated during cracking of calabash seed oil at 380 °C for 2 h using total liquid yield (TLY), total petroleum hydrocarbons (TPH), and hydrocarbon carbon-range distribution as performance indicators. XRF confirmed Ni and Cr incorporation, while XRD showed preservation of the crystalline aluminosilicate framework with metal loading. FTIR further indicated retention of surface hydroxyl functionalities and interactions between the supported metal species and the aluminosilicate surface. NiCr incorporation substantially enhanced the textural properties, increasing the BET surface area from 167.73 to 252.70 m²/g for NiCr/ATC and from 188.20 to 314.00 m²/g for NiCr/BTC. However, catalytic performance showed that surface area alone did not explain product distribution. The results indicate that catalyst performance was governed by the combined effects of textural properties, active-site accessibility, support chemistry, and Ni–Cr-induced surface functionality. The high heavier-hydrocarbon fractions also suggest secondary reactions, including possible oligomerization, condensation, cyclization, or incomplete cracking. Overall, the study shows locally sourced Ogbunike clay as a potential catalyst support for converting non-edible calabash seed oil into hydrocarbon products relevant to sustainable aviation fuel, while highlighting the need for further optimization of catalyst acidity, metal dispersion, and pore architecture to improve C8–C16 selectivity.
**Keywords:** Aviation biofuel, Activated Clays, Catalyst synthesis, FTIR, XRD, XRF, SEM

## 1. Introduction

Due to the significant role of air transportation in the modern world, the aviation industry is expected to continue expanding in the coming years, leading to increased consumption of aviation fuel. Conventional aviation fuel is fossil-based and notorious for its greenhouse gas (GHG) emissions. Hence, the amount of anthropogenic carbon dioxide ($CO_2$) in the atmosphere due to this sector's activities will increase each year as the aviation industry expands (Yang et al., 2019). According to Alherbawi et al. (2021), the aviation sector contributes about 2.6 % of global $CO_2$ emissions, which is predicted to reach 5 % in 2050 due to the continuous rise in aviation activities. Apart from the environmental issues imposed by the use of fossil-based aviation fuel, another problem faced by this sector is the finite nature of fossil fuels (Yang et al., 2019). In light of this, a sustainable aviation biofuel that has little or no adverse environmental impact is of the utmost importance. Such fuel should be able to use renewable feedstock, reduce dependence on fossil fuels, and emit little or no GHG during combustion. It must possess good cold flow properties, a low freezing point, and good thermal stability (Zhao et al., 2019). To satisfy these requirements, the feedstock for renewable aviation biofuel should be of biological origin (Mofijur et al., 2023) and second-generation, to avoid competition with the food market (Walls & Rios-Solis, 2020). This has intensified research on sustainable aviation biofuel (SAF) production from natural (organic) sources to reduce the aviation sector's carbon emissions. Since organic materials absorb $CO_2$ as they grow, they are capable of reducing the amount of lifecycle $CO_2$ emitted by approximately 80 %; some of the sustainable fuels produced from these feedstocks contain minimal aromatics and impurities such as soot and sulfur and hence can reduce the intensity of aviation's non-$CO_2$ climate impacts (Lim et al., 2023). The International Air Transport Association (IATA) estimates that SAF could contribute around 65% of the emissions reduction needed by aviation to reach net-zero $CO_2$ emissions in 2050 (IATA, 2026). As a result, many biomass feedstocks have been investigated for aviation biofuel production. Biomass feedstocks include dedicated energy crops, agricultural crop residues, municipal waste, forestry residues, algae, and wood processing residues. These biomasses contain organics such as lignocellulose, starch, fats and oils, and sugars, which can be converted into biomass- derived fuels via various production pathways (Kim et al., 2018).

Among the various production pathways for aviation biofuel from biomass, seven have been specified in ASTM D7566 to produce drop-in SAFs (IATA 2026b). These include: Fischer-Tropsch synthesis (FT), Fischer-Tropsch synthesis with aromatics (FT-SPK/A), Hydroprocessing of esters and fatty acids (HEFA), Direct sugar to hydrocarbons producing synthetic iso-paraffins (SIP), Alcohol-to-Jet (AJT), Catalytic hydrothermolysis Jet fuel (CHJ) and Hydroprocessed hydrocarbons (HC-HEFA or HH-SPK (IATA 2026b). Although some of these processing routes have reached industrial piloting stages, they are yet to provide a practical and economically competitive alternative energy source to replace fossil-based aviation fuel. Hence, a call for further research. Of all the certified routes, HEFA using oily feedstocks is the most promising route for aviation biofuel production, and has been predicted to predominate over other processing routes soon due to its relative simplicity (Yang et al., 2019), relatively low production cost and low GHG emissions (Ng et al., 2021). Notwithstanding these merits, this production route has some challenges, which include the use of costly feedstocks (edible oil) and the lack of cost effective and environmentally friendly catalyst, which has high selectivity for desired products. Over the years, the feasibility of using low-cost feedstocks, such as camelina, jatropha curcas (Patil & Vaidya, 2018), and karanja oil in biodiesel fuel production via the deoxygenation process has been investigated.

The HEFA processing route consists of two reaction stages: deoxygenation and cracking/isomerisation reaction stages. The deoxygenation stage involves the removal of oxygen via three possible reaction paths: hydrodeoxygenation (HDO), decarbonylation (DCO), and decarboxylation ($DCO_2$). Unfortunately, the HDO pathway, which represents the most developed route and which forms the basis of several commercialized processes for jet biofuel production from oil feedstocks (Santillan-Jimenez et al., 2014), requires high $H_2$ pressure (300-420 $m^3H_2/m^3$oil) (Jeon et al., 2019), use of precious metal catalysts, and specialized and expensive equipment (Mahene et al., 2023). To avoid these problems, researchers are focusing on developing catalysts with high selectivity for the decarboxylation/decarbonylation (deCOx) route in the deoxygenation of triglycerides, which does not require high $H_2$ input. Hence, catalyst design remains the controlling factor for efficient SAF production from vegetable oils. The production of aviation biofuels involves complex conversion pathways that require multiple catalytic reactions. Conventional catalytic systems often employ separate catalysts for hydrodeoxygenation, hydrocracking, isomerization, and aromatization. Such approaches increase process complexity, operational costs, and energy requirements. Multifunctional catalysts have emerged as an innovative solution by integrating different catalytic functionalities within a single catalyst structure. These catalysts enable simultaneous reactions, thereby improving conversion efficiency and product selectivity.

Previous studies on the deoxygenation of triglyceride-based feedstocks for renewable fuel production have predominantly employed monometallic catalysts, such as Ni, Pt, Pd and Rh, as well as bimetallic catalysts in sulfided and non-sulfided forms, including $NiMoS_2$, $CoMoS_2$, $NiWS_2$, NiMo, CoMo, PdCu and PdNi. These catalysts have been investigated using various support materials, including metal oxides and mixed oxides, mesoporous materials, activated carbon and zeolites (Cheah et al., 2022; Khan et al., 2019; Zhao et al., 2019). Despite these advances, there remains a need to explore alternative, cost-effective and locally available clay-based catalyst systems for the direct conversion of triglyceride-rich feedstocks into aviation-range hydrocarbons. To the best of the authors' knowledge, the application of acid- and alkali-activated Ogbunike clay-supported NiCr bimetallic catalysts for the single-pot production of aviation biofuel from calabash seed oil has not been previously reported. Accordingly, the novelty of this research lies in the development and application of a NiCr bimetallic catalytic system derived from locally sourced Ogbunike clay for the single-pot catalytic upgrading of calabash seed oil into aviation biofuel. The study encompasses the acid and alkaline activation of the clay, incorporation of NiCr active metal species through impregnation, comprehensive physicochemical characterization of the synthesized catalysts, and evaluation of their catalytic performance in the conversion of calabash seed oil to aviation-range hydrocarbons.

## 2.0 Materials and methods

### 2.1 Sample Collection

The clay was collected from the Ogbunike community in Idemili North L.G.A., Anambra state, Nigeria. The non-edible oil used was extracted from calabash seed. The extraction process and the properties of the seed oil were reported elsewhere (Ejiofor et al., 2026). All other chemicals were purchased at their analytical grade from the chemicals and drug market, Bridge Head Onitsha, Anambra State, Nigeria.

### 2.2 Preparation of Acid–treated Clay and Alkaline-treated Clay

The Ogbunike clay was dried in an oven at a temperature of 100 **℃** for 2 h, crushed, sieved using a 200-mesh sieve, and stored in a tight container for the synthesis of acid-treated clay (ATC) and alkaline-treated clay (BTC). The ATC and BTC was prepared from Ogbunike clay following the method described by Wang et al. (2017). To prepare ATC, 100 g of the Ogbunike clay was first calcined in a muffle furnace at 800 **℃** for 1 h and then added to 300 ml of 2 M HCl. These were allowed to react with continuous stirring at 90 **℃** for 5 h. The mixture was then washed with distilled water to remove $Cl^-$ (tested with silver nitrate, $AgNO_3$ solution) and dried in an oven at 120 **℃** for 3 h. The final product was stored in a container and labelled as ATC.

A Similar procedure was followed in preparing BTC from Ogbunike clay. About 100 g of the natural clay was calcined in a muffle furnace at 1000 **℃** for 1 h and then added to 312.5 ml of 4 M NaOH. The mixture was allowed to react with stirring at 95 **℃** for 2 h. The resulting product was washed repeatedly with distilled water until its alkalinity was substantially reduced, as confirmed using litmus paper. The washed product was subsequently filtered, oven-dried at 120 °C for 3 h, and labeled as BTC.

### 2.3 Incorporation of Catalyst Precursors

Two supported bimetallic catalysts (NiCr/ATC and NiCr/BTC) were prepared via the wet impregnation method. Nickel nitrate ($Ni(NO_3)_2.6H_2O$) and chromium nitrate ($Cr(NO_3)_3.9H_2O$) were used as the metal precursors. The procedure followed the method described by Liu et al. (2014) with slight modifications. The metal precursors in a ratio of 2:1 (nickel nitrate: chromium nitrate) were dissolved in deionized water and then added separately to each of the support solutions. The ratio of metal to support is 1: 8. The mixture was stirred at 40 **℃** for 1 h, followed by dehydration at 100 **℃** for 3 h. Finally, the catalysts were calcined at 550 **℃** for 3 h.

### 2.4 Catalyst Characterization

The specific surface area and pore size of the synthesized catalysts were determined using BET and DFT methods of $N_2$ adsorption isotherm, respectively. FTIR spectrometer was used to characterize the functional groups. X-ray fluorescence (XRF) and X-ray diffraction (XRD) were employed to determine the chemical composition, the phase composition, and the crystal structure of the synthesized catalysts, respectively.

### 2.5 Catalysts' activity Evaluation

The synthesized catalysts were tested for their ability to promote one-pot production of bio-aviation fuel from calabash seed oil. Following the method described by Uzochukwu et al. (2025) with slight modification, the catalytic cracking was conducted using the prepared catalysts. In each case, the reactor was loaded with 10 ml of the oil and the catalyst (2 g). the system temperature is increased gradually by 10 **℃** $min^{-1,}$ and the liquid product recovered as the reaction progresses. The stepwise temperature increase continued until the system reaches the desired reaction temperature (380 **℃**). The system is then maintained at this temperature for the rest of the reaction time (2 h). Once the reaction time is completed, the recovered liquid product is centrifuged to separate any dissolved solid catalysts from the liquid phase product. The volume of the liquid product was recorded and the liquid product analysed using Gas Chromatography-Flame Ionization Detector (GC-FID). The result was used to investigate the catalyst activity via jet fuel-range alkane selectivity, diesel-range alkane selectivity, and total liquid yield, as shown in equations 1 – 3, respectively (Praikaew et al., 2024).

$$Jet\ fuel-range\ alkane\ selectivity\ (\%) = \frac{Total\ weight\ of\ C_8\ to\ C_{16}\ in\ product\ (g)}{Total\ weight\ of\ \ TG\ converted\ \ (g)} X\ 100 \quad (1)$$

$$Diesel-range\ alkane\ selectivity\ (\%) = \frac{Total\ weight\ of\ C_{16}\ to\ C_{18}\ in\ product\ (g)}{Total\ weight\ of\ TG\ converted\ (g)} X\ 100 \quad (2)$$

$$Total\ liquid\ yield\ (\%) = \frac{Total\ weight\ of\ product\ (g)}{Total\ weight\ of\ feed\ (g)} X\ 100 \quad (3)$$

## 3.0 Result and Discussion

### 3.1 X-ray Fluorescence (XRF) Analysis of the Prepared Catalysts

The oxide compositions of the acid-treated clay (ATC), base-treated clay (BTC), and the corresponding NiCr-impregnated catalysts were determined by X-ray fluorescence (XRF). The analysis was carried out to evaluate the chemical composition of the catalyst supports and confirm the successful incorporation of nickel and chromium as active catalytic species. The XRF results presented in Table 1 reveals that there are significant variations in the oxide composition as a result of metal impregnation. This indicates that metal impregnation altered the chemical characteristics of the catalyst materials.

Silicon dioxide ($SiO_2$) was the dominant oxide in the catalyst supports, confirming that silica constitutes the principal structural framework of the prepared materials. The $SiO_2$ concentrations of ATC and BTC are 31.101 wt.% and 23.234 wt.%, respectively, indicating that both treated clay materials retained the aluminosilicate structure of the clay mineral. After nickel-chromium impregnation, the $SiO_2$ concentration decreased to 24.440 wt.% in NiCr/ATC and 15.452wt.% in NiCr/BTC. The decrease in $SiO_2$ concentration following NiCr incorporation is therefore interpreted primarily as a compositional dilution effect arising from the addition of Ni- and Cr-containing oxide species to the catalyst matrix. The incorporation of these active phases increases their relative contribution to the total catalyst mass and consequently reduces the calculated $SiO_2$ fraction. This

interpretation aligns with previous studies of impregnated $Ni/SiO_2$ catalysts, in which nickel precursor species are deposited onto silica and converted to supported NiO phases during calcination (Yamashita et al., 2015).

The presence of aluminium oxide ($Al_2O_3$) in the synthesized catalysts confirms the aluminosilicate nature of the clay minerals. Alumina is an important structural oxide that contributes to catalyst mechanical strength, and thermal stability (Busca et al., 2024). ATC contained 8.012 wt.% $Al_2O_3$, whereas BTC contained 5.278 wt.%. Following NiCr impregnation, the alumina content remained relatively stable, suggesting that the impregnation process deposited metal oxides primarily on the catalyst surface without significantly altering the clay framework.

Iron oxide ($Fe_2O_3$) was one of the major oxides detected in all catalysts, with concentrations ranging from 3.220 to 18.067 wt.%. Iron naturally occurs in clay minerals and can influence catalytic behaviour by participating in oxidation–reduction reactions and facilitating oxygen mobility (Busca et al., 2024).

Copper oxide (CuO), zinc oxide (ZnO), titanium dioxide ($TiO_2$), manganese oxide (MnO), cobalt oxide ($Co_3O_4$), Silver oxide ($Ag_2O$), zirconium oxide ($ZrO_2$) and other minor oxides were also identified in varying proportions. CuO concentrations were highest in ATC (7.354 wt.%) but decreased after metal impregnation, indicating partial redistribution of copper species. Zinc oxide remained relatively abundant in BTC (14.056 wt.%), while $ZrO_2$ increased substantially in NiCr/BTC. The variations in the concentrations of minor oxides after metal incorporation may partly be due to metal–support interactions and changes in the relative composition of the catalyst materials. During impregnation and subsequent thermal treatment, the introduced metal species may interact with silica, alumina and other mineral constituents of the support, potentially resulting in the formation of interfacial compounds or mixed oxide phases (Lokteva & Golubina, 2019; Busca et al., 2024).

Nickel oxide (NiO) and chromium oxide ($Cr_2O_3$) are the principal active catalytic phases introduced during catalyst impregnation. The supports (ATC and BTC) contained only trace quantities of NiO and $Cr_2O_3$, indicating the absence of significant naturally occurring nickel and chromium species. Following impregnation, both oxides increased substantially. NiCr/BTC contained the highest NiO concentration (3.489 wt.%). Nickel is widely recognized as one of the most active and economical transition metal catalysts for deoxygenation of triglycerides (Santillan-Jimeneze et al., 2014), while Chromium can act as a structural promoter in Ni-based catalysts by modifying the dispersion and spatial distribution of Ni species, enhancing Ni–support interactions, and inhibiting Ni particle growth and sintering during high-temperature operation (Zhu et al., 2024; Al-Fatesh et al., 2020; Gonzalez et al., 2020). Therefore, the observed increase in NiO and $Cr_2O_3$ confirms the successful deposition of nickel and chromium onto the catalyst supports and indicates the presence of catalytically active phases. Other minor oxides were identified in varying proportion in the synthesized catalysts.

Table 1: The Oxide table of XRF Characterisation of the Prepared Catalysts

| **OXIDE** | **CONCENTRATION (wt%)** | | | |
|---|---|---|---|---|
| | **ATC** | **BTC** | **NiCr/ATC** | **NiCr/BTC** |
| $SiO_2$ | 31.101 | 23.234 | 24.440 | 15.452 |
| $V_2O_5$ | 0.043 | 0.023 | 0.254 | 0.206 |
| $Cr_2O_3$ | 0.022 | 0.010 | 0.089 | 0.103 |
| MnO | 0.012 | 5.054 | 5.278 | 5.378 |
| $Fe_2O_3$ | 9.022 | 7.436 | 6.467 | 12.109 |
| $Co_3O_4$ | 0.012 | 0.010 | 0.078 | 0.000 |
| NiO | 0.010 | 0.167 | 0.024 | 3.489 |
| CuO | 7.354 | 4.894 | 3.167 | 2.616 |
| $Nb_2O_3$ | 0.003 | 0.010 | 0.108 | 0.054 |
| $WO_3$ | 0.027 | 0.017 | 0.046 | 0.045 |
| $P_2O_5$ | 0.000 | 0.894 | 0.028 | 0.026 |
| $SO_3$ | 7.012 | 7.978 | 2.178 | 6.108 |
| CaO | 13.120 | 11.898 | 10.232 | 0.167 |
| MgO | 14.221 | 9.167 | 7.478 | 10.178 |
| $K_2O$ | 2.103 | 1.378 | 15.676 | 1.107 |
| BaO | 0.023 | 0.127 | 0.189 | 0.203 |
| $Al_2O_3$ | 8.012 | 5.278 | 2.129 | 2.565 |
| $Ta_2O_5$ | 0.022 | 0.000 | 0.033 | 0.178 |
| $TiO_2$ | 0.401 | 1.433 | 5.887 | 10.030 |
| ZnO | 5.072 | 14.056 | 5.189 | 8.454 |
| $Ag_2O$ | 0.267 | 5.867 | 0.034 | 0.000 |
| Cl | 1.462 | 1.467 | 7.054 | 2.565 |
| $ZrO_2$ | 0.000 | 3.456 | 0.078 | 10.672 |
| $SnO_2$ | 0.012 | 0.023 | 0.675 | 0.000 |
| PbO | 0.667 | 2.067 | 3.189 | 2.443 |

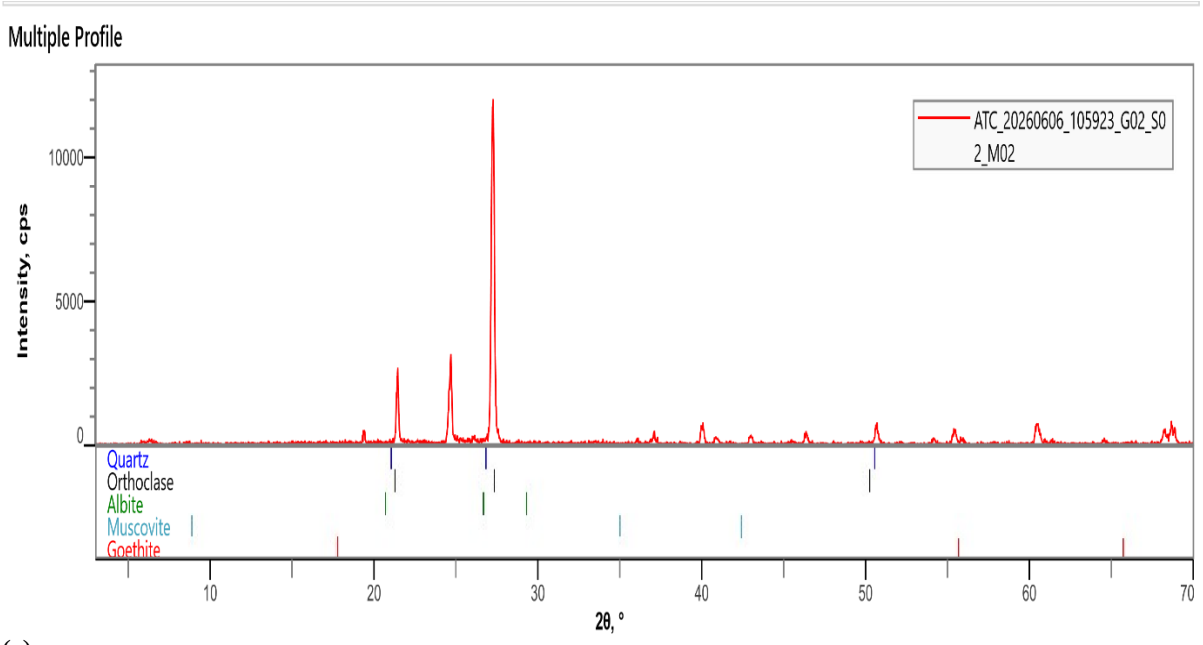


(a)

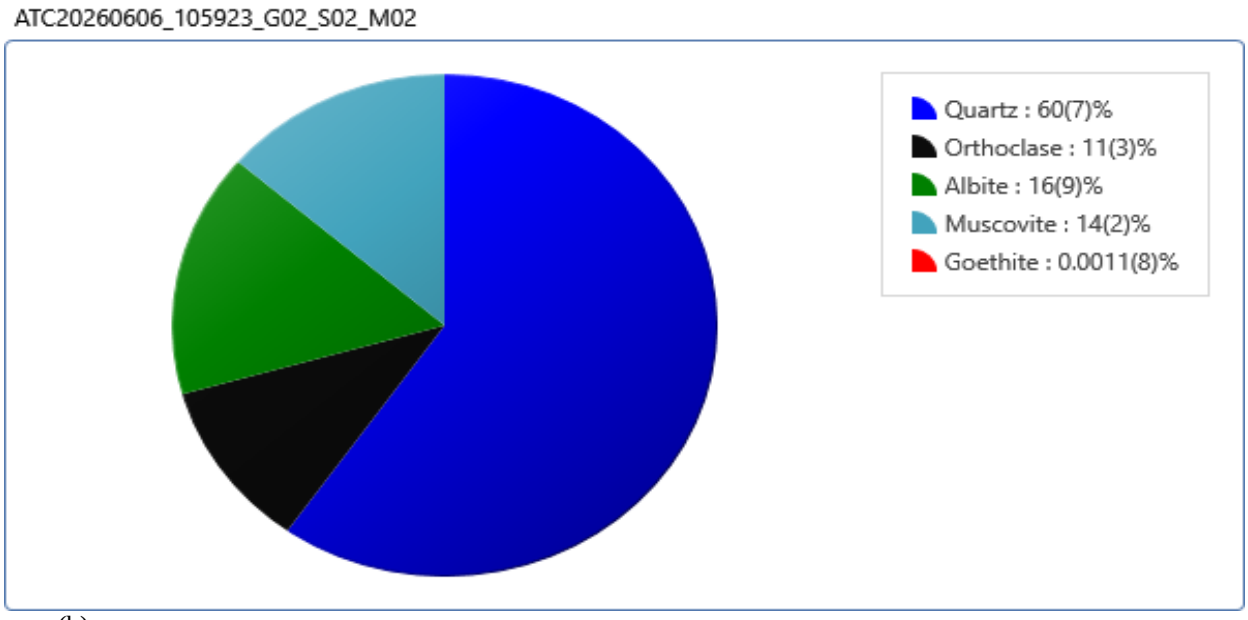


(b)

Figure 1: X-ray diffraction of ATC: (a) the diffractogram, (b) the phase-percentage chart

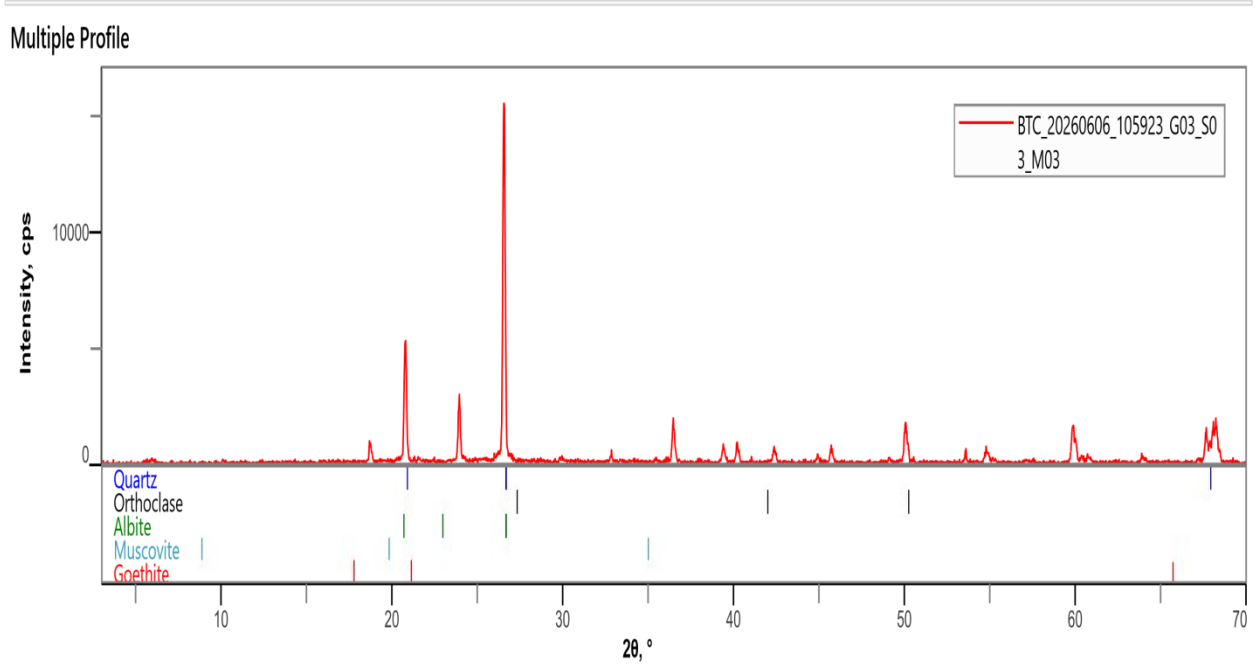


(a)

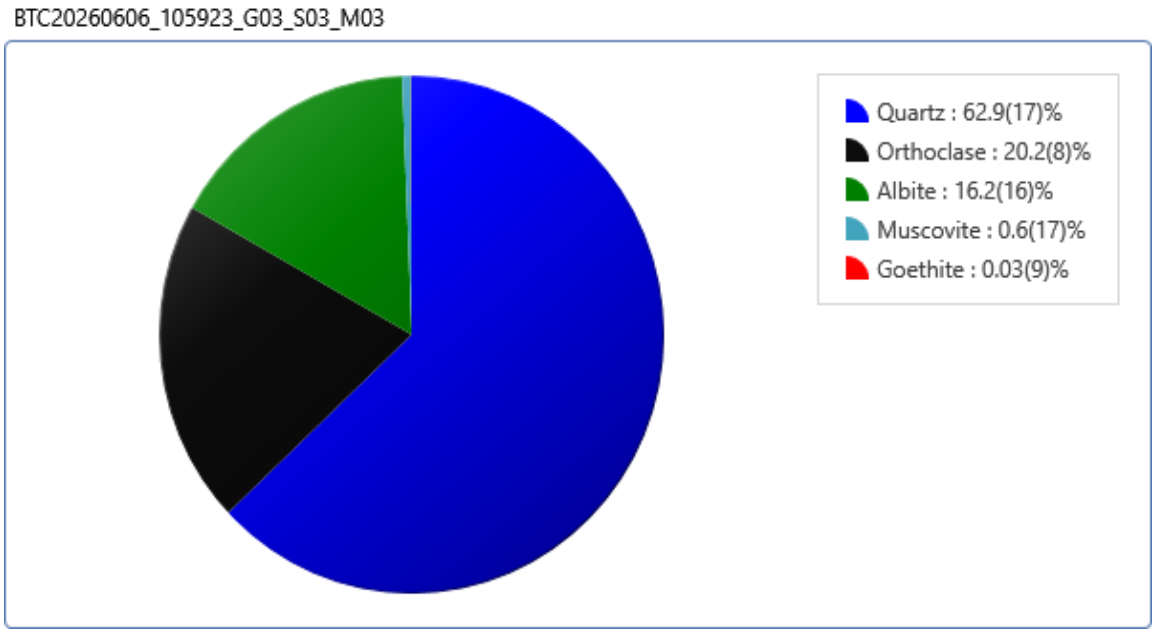


(b)

Figure 2: X-ray diffraction of BTC: (a) the diffractogram, (b) the phase-percentage chart

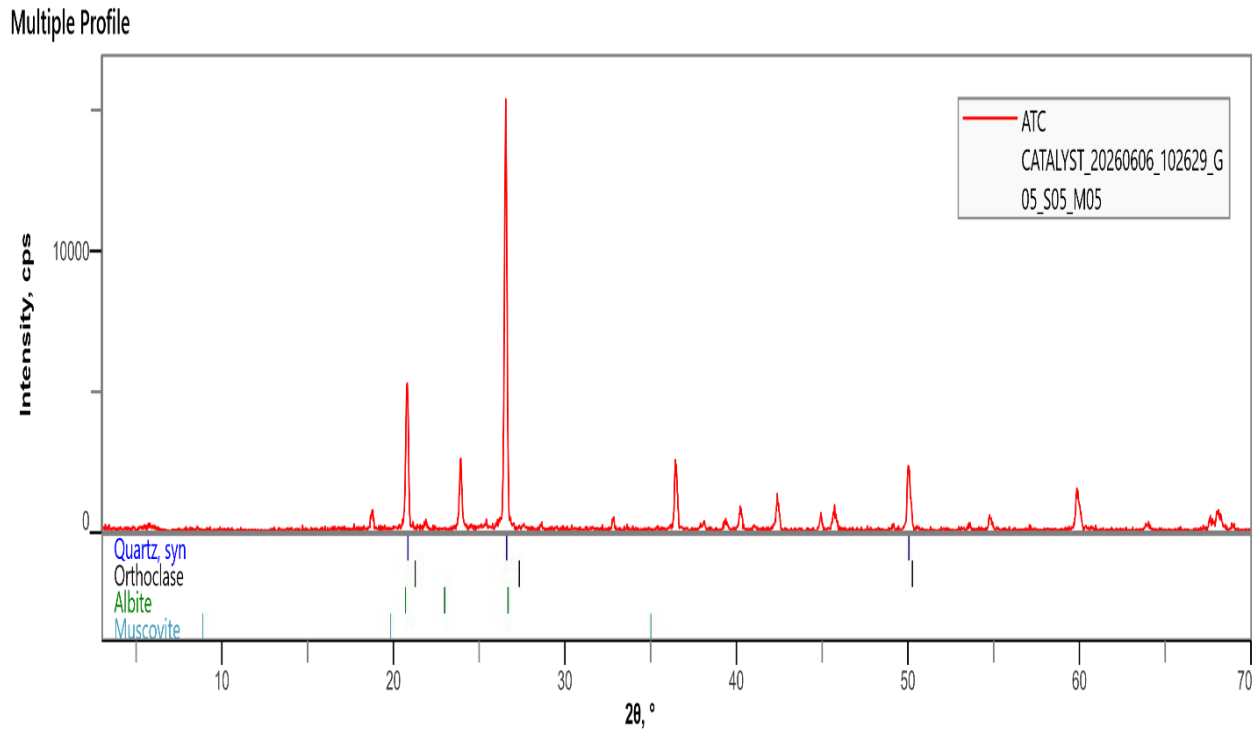


(a)

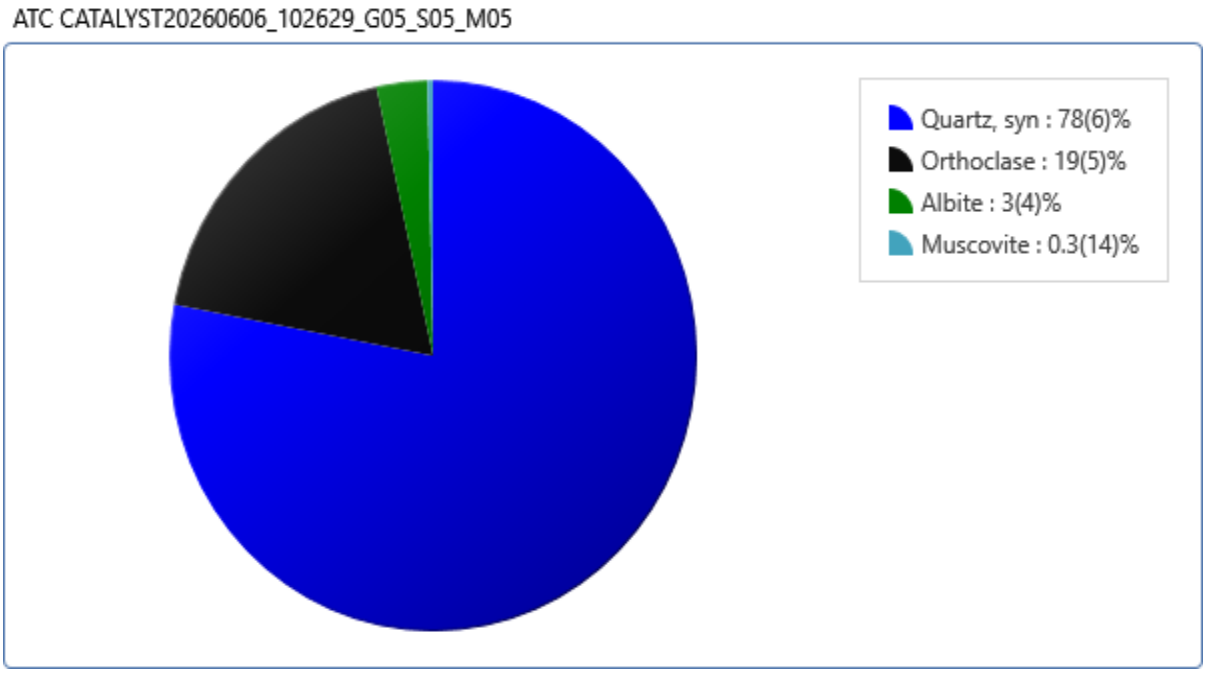


(b)

Figure 3: X-ray diffraction of NiCr/ATC: (a) the diffractogram, (b) the phase-percentage chart

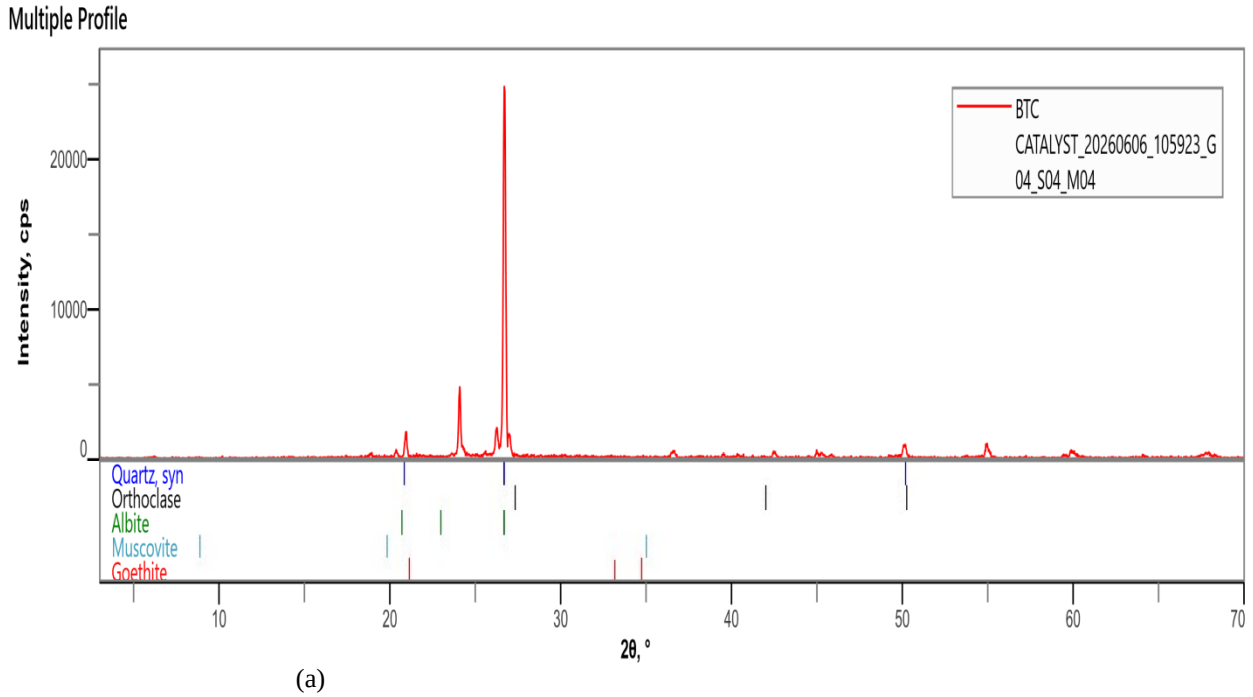


(a)

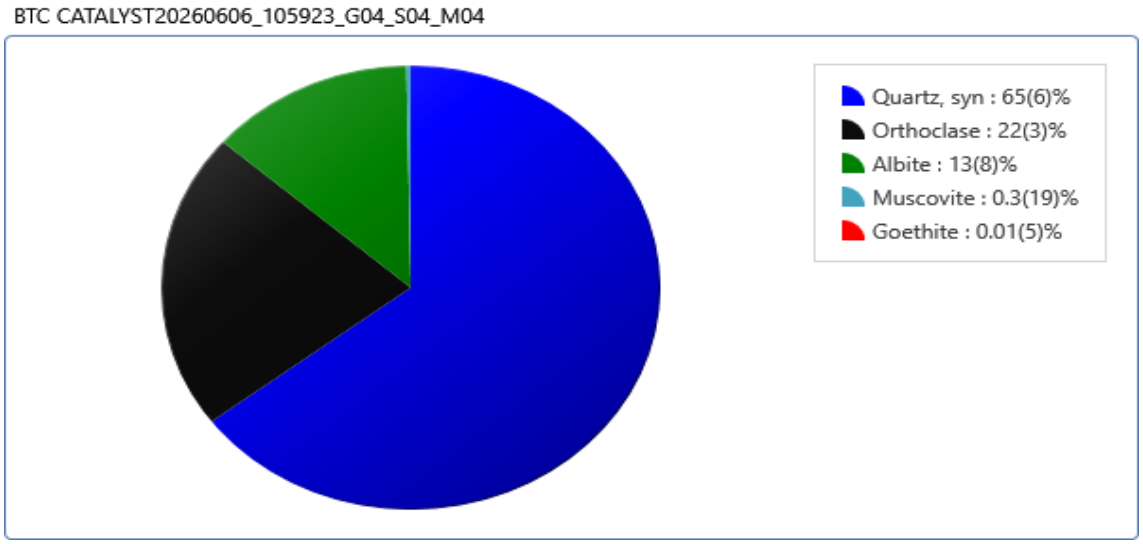


(b)

Figure 4: X-ray diffraction of NiCr/BTC: (a) the diffractogram, (b) the phase-percentage chart

Table 2: The Peak list for ATC diffractogram

| Pos. [°2Th.] | Height [cts] | FWHM Left [°2Th.] | d-spacing [Å] | Rel. Int. [%] |
|---|---|---|---|---|
| 6.4498 | 5.59 | 0.7872 | 13.70416 | 0.92 |
| 19.3834 | 22.99 | 0.1181 | 4.57947 | 3.79 |
| 21.4397 | 156.65 | 0.1378 | 4.14467 | 25.83 |
| 24.6647 | 175.58 | 0.1181 | 3.60957 | 28.95 |
| 27.2976 | 606.47 | 0.2165 | 3.26709 | 100.00 |
| 37.0657 | 25.14 | 0.1181 | 2.42549 | 4.14 |
| 39.9694 | 35.09 | 0.1968 | 2.25572 | 5.79 |
| 40.8705 | 13.63 | 0.2362 | 2.20805 | 2.25 |
| 43.0106 | 16.24 | 0.1574 | 2.10301 | 2.68 |
| 46.3447 | 19.82 | 0.2362 | 1.95919 | 3.27 |
| 50.6313 | 38.83 | 0.1574 | 1.80292 | 6.40 |
| 54.1561 | 9.82 | 0.2362 | 1.69361 | 1.62 |
| 55.4326 | 25.64 | 0.2362 | 1.65760 | 4.23 |
| 60.3953 | 36.44 | 0.2755 | 1.53272 | 6.01 |
| 68.7082 | 31.98 | 0.2362 | 1.36617 | 5.27 |

Table 3: The Peak List for BTC diffractogram

| Pos. [°2Th.] | Height [cts] | FWHM Left [°2Th.] | d-spacing [Å] | Rel. Int. [%] |
|---|---|---|---|---|
| 5.8934 | 7.03 | 0.4723 | 14.99669 | 0.76 |
| 18.7229 | 46.81 | 0.1574 | 4.73950 | 5.08 |
| 20.7959 | 315.13 | 0.1771 | 4.27151 | 34.23 |
| 23.9522 | 153.29 | 0.1378 | 3.71530 | 16.65 |
| 26.5561 | 920.73 | 0.1771 | 3.35662 | 100.00 |
| 29.9531 | 8.50 | 0.4723 | 2.98323 | 0.92 |
| 32.8205 | 17.98 | 0.1181 | 2.72885 | 1.95 |
| 36.4364 | 98.72 | 0.1378 | 2.46592 | 10.72 |
| 39.3861 | 42.89 | 0.1574 | 2.28778 | 4.66 |
| 40.1948 | 47.19 | 0.1574 | 2.24360 | 5.13 |
| 42.3565 | 36.18 | 0.1968 | 2.13396 | 3.93 |
| 44.9048 | 16.01 | 0.2362 | 2.01861 | 1.74 |
| 45.6914 | 34.83 | 0.1574 | 1.98567 | 3.78 |
| 50.0439 | 101.62 | 0.1378 | 1.82270 | 11.04 |
| 53.5619 | 29.25 | 0.1574 | 1.71099 | 3.18 |
| 54.7494 | 30.44 | 0.1968 | 1.67665 | 3.31 |
| 59.8646 | 96.18 | 0.1181 | 1.54504 | 10.45 |
| 63.9559 | 10.12 | 0.2362 | 1.45572 | 1.10 |
| 67.6302 | 81.49 | 0.1181 | 1.38529 | 8.85 |
| 68.2333 | 92.26 | 0.1181 | 1.37452 | 10.02 |

Table 4: The Peak List for The NiCr/ATC Diffractogram

| Pos. [°2Th.] | Height [cts] | FWHM Left [°2Th.] | d-spacing [Å] | Rel. Int. [%] |
|---|---|---|---|---|
| 5.7367 | 5.65 | 0.9446 | 15.40593 | 0.62 |
| 18.7503 | 39.16 | 0.1574 | 4.73264 | 4.29 |
| 20.8371 | 276.17 | 0.1771 | 4.26315 | 30.23 |
| 21.8733 | 11.30 | 0.2362 | 4.06347 | 1.24 |
| 23.9038 | 128.13 | 0.0984 | 3.72271 | 14.02 |
| 26.5402 | 913.62 | 0.1771 | 3.35859 | 100.00 |
| 32.7998 | 23.83 | 0.1574 | 2.73053 | 2.61 |
| 36.3991 | 129.52 | 0.0984 | 2.46836 | 14.18 |
| 38.0285 | 12.58 | 0.3149 | 2.36627 | 1.38 |
| 39.3569 | 17.76 | 0.2362 | 2.28940 | 1.94 |

| | | | | |
|---|---|---|---|---|
| 40.2230 | 41.98 | 0.1968 | 2.24209 | 4.60 |
| 42.3712 | 66.64 | 0.1968 | 2.13325 | 7.29 |
| 44.9124 | 32.94 | 0.1181 | 2.01828 | 3.61 |
| 45.6772 | 43.62 | 0.2362 | 1.98625 | 4.77 |
| 49.9699 | 122.12 | 0.0787 | 1.82522 | 13.37 |
| 54.7429 | 28.17 | 0.2362 | 1.67684 | 3.08 |
| 59.8210 | 80.34 | 0.1574 | 1.54606 | 8.79 |
| 63.9408 | 9.70 | 0.2362 | 1.45602 | 1.06 |
| 68.0975 | 33.91 | 0.2362 | 1.37692 | 3.71 |

Table 5: The peak list for the NiCr/BTC Diffractogram

| Pos. [°2Th.] | Height [cts] | FWHM Left [°2Th.] | d-spacing [Å] | Rel. Int. [%] |
|---|---|---|---|---|
| 20.3604 | 27.23 | 0.1574 | 4.36188 | 1.85 |
| 20.9414 | 92.20 | 0.1378 | 4.24215 | 6.27 |
| 24.0800 | 278.14 | 0.1378 | 3.69586 | 18.92 |
| 26.2426 | 109.85 | 0.1574 | 3.39599 | 7.47 |
| 26.6786 | 1469.87 | 0.1574 | 3.34148 | 100.00 |
| 36.6142 | 24.15 | 0.2755 | 2.45435 | 1.64 |
| 42.4541 | 24.17 | 0.1574 | 2.12928 | 1.64 |
| 44.9626 | 23.14 | 0.1574 | 2.01615 | 1.57 |
| 50.1075 | 46.73 | 0.1968 | 1.82053 | 3.18 |
| 54.8933 | 48.08 | 0.1968 | 1.67260 | 3.27 |
| 59.9309 | 22.73 | 0.3149 | 1.54349 | 1.55 |
| 67.7018 | 15.66 | 0.6298 | 1.38401 | 1.07 |

### 3.2 X-ray Diffraction (XRD) Analysis of synthesized catalysts

X-ray diffraction (XRD) analysis was performed to investigate the crystalline phases, and the crystallinity of the synthesized catalyst supports, and the corresponding NiCr supported catalysts. The nickel/chromium impregnation was intended to introduce catalytically active sites without significantly disrupting the crystalline framework. The various XRD diffractograms and phase-percentage charts, with the corresponding peak lists for these catalysts are presented in Figure 1-4 and Table 2-5, respectively. The diffraction patterns demonstrate that all catalysts retained well-defined crystalline structures after metal loading, indicating that the preparation procedures preserved the structural integrity of the supports

#### 3.2.1: XRD Analysis of ATC

The XRD pattern of ATC (Figure 1) exhibits several sharp diffraction peaks characteristic of a highly crystalline aluminosilicate material. The most intense reflection is observed around $2\theta \approx 27.2°$, which is assigned to the (101) plane of α-quartz ($SiO_2$). Besides quartz, the lower-intensity reflections were assigned to feldspar minerals, including albite and orthoclase, as well as muscovite and trace goethite. The presence of aluminosilicate phases, particularly the clay/micaceous components, provides Si–O–Al environments and surface hydroxyl groups capable of contributing Brønsted and Lewis acid sites. Such acidic functionalities are important in the activation of oxygen-containing molecules and C–O bonds during catalytic upgrading and hydrodeoxygenation reactions (McCabe &

Adams, 2013; Wang et al., 2013). The sharpness and narrow width of the quartz reflections indicate a relatively high degree of crystallinity, suggesting that the activation process preserved the crystalline framework while removing amorphous impurities. Generally, high crystallinity promotes thermal stability and mechanical resistance, both of which are essential for catalysts operating under high processing conditions exceeding 350–450 **℃** (Zhou et al., 2025).

### 3.2.2 XRD Analysis of BTC

BTC exhibits diffraction peaks similar to those observed for ATC. This is expected since both catalyst supports originate from the same clay minerals. However, the quartz reflections appear relatively more intense, reflecting the higher quartz content reported by the phase analysis (Figure 2). The principal quartz peak near 26.6° (101) dominates the diffractogram; additional reflections at approximately 20.8°, 36.5°, 39.4°, 40.2°, 45.7 °, 50.0°, 55.7°, 59.8°, and 63.9° further confirm the predominance of crystalline quartz in the catalyst support. Also, additional peaks associated with orthoclase and albite remain evident. The reduction in muscovite-related reflections compared with ATC suggests that alkaline treatment altered the layered mica structure, leading to a more stable crystalline framework. The persistence of strong quartz reflections confirms that silica remained chemically stable throughout catalyst preparation. The overall diffraction profile reveals that BTC possesses adequate crystallinity and structural integrity. Hence, it's expected to maintain its textural properties during repeated heating and reaction cycles.

### 3.2.3 XRD Analysis of NiCr/ATC

The XRD pattern of NiCr/ATC (Figure 3) shows that upon impregnation with nickel and chromium salts and subsequent calcination, the catalyst retains all major quartz reflections, indicating that incorporation of the active metals did not destroy the crystalline aluminosilicate framework. The dominant quartz reflection at approximately 26.6° remains the most intense diffraction peak, showing that the silica matrix retained its structural stability after catalyst synthesis. Compared with the parent ATC support, some of the weaker reflections assigned to albite and muscovite exhibit reduced intensity following metal incorporation. This change may be associated with partial masking or dilution of the crystalline phases by the deposited metal species, as well as structural or phase rearrangements induced during calcination. Similar changes in XRD patterns have been reported for impregnated clay- and alumina-supported metal catalysts, where calcination promotes interactions between the deposited metal oxides and the support, sometimes resulting in changes in phase composition, metal dispersion and the relative intensity of characteristic diffraction reflections (Gonzalez et al., 2025; He et al., 2021).

A particularly significant feature of the diffractogram is the absence of distinct diffraction peaks corresponding to crystalline nickel oxide or chromium oxide. Typical reflections of NiO occur near 37.2°, 43.3°, 62.9°, 75.4° and 79.4°, whereas $Cr_2O_3$ generally exhibits reflections around 24.5°, 33.6°, 36.2°, 41.5°, 50.2° and 54.9°. Their absence suggests that nickel and chromium species are highly dispersed on the catalyst surface, possess very small crystallite sizes below the XRD detection limit, or exist as poorly crystalline or amorphous phases.

High metal dispersion is beneficial because catalytic reactions occur on exposed metal atoms rather than within large crystalline particles. Strong metal–support interaction suppresses particle agglomeration during calcination, thereby increasing the number of accessible active sites available for deoxygenation, cracking and isomerisation reactions.

### 3.2.4 XRD Analysis of NiCr/BTC

The XRD diffractogram of NiCr/BTC also preserves the characteristic reflections of quartz, orthoclase and albite, demonstrating that the BTC support remained structurally stable after nickel–chromium loading. Unlike NiCr/ATC, only slight changes in peak intensity are observed, suggesting that BTC experienced minimal structural modification during impregnation.

Again, no intense crystalline NiO or $Cr_2O_3$ reflections are observed. This indicates effective dispersion of the active metal species throughout the catalyst surface. The retention of sharp quartz peaks together with the absence of large metal oxide crystallites suggests strong anchoring of nickel and chromium within the aluminosilicate matrix.

Comparison of the support materials with the metal-loaded catalysts reveals that the characteristic quartz reflections remain essentially unchanged after impregnation, confirming that the silica framework is chemically stable during catalyst preparation. The reductions in the intensity of feldspar and mica reflections after metal loading suggest that nickel and chromium species are preferentially deposited on these aluminosilicate surfaces.

The absence of newly formed crystalline metal oxide phases, despite successful impregnation, provides indirect evidence of strong metal–support interaction. Strong interactions inhibit migration and sintering of metal particles during calcination and generally lead to higher catalytic activity because more active sites remain exposed (Zhang et al., 2018).

In relation to aviation biofuel production, the structural characteristics revealed by XRD are highly desirable for catalysts intended for deoxygenation of vegetable oils into sustainable aviation fuel. High crystallinity ensures excellent thermal stability under severe reaction conditions, while highly dispersed nickel and chromium species provide abundant active sites for hydrogenation, decarboxylation and hydrodeoxygenation reactions. Furthermore, preservation of the aluminosilicate framework ensures that acidic sites remain available for cracking and isomerisation reactions that improve jet fuel quality.

### 3.3 FTIR Analysis of the Synthesised Catalysts

The FTIR spectral interpretations for the synthesised catalysts are presented in Tables 6-9. The spectra revealed several characteristic absorption bands corresponding to hydroxyl groups, carbonate species, adsorbed moisture, aliphatic functional groups, and metal–oxygen interactions. Although peak intensities differed among the catalysts, most spectra showed similar absorption regions, suggesting comparable surface functional groups, with modifications arising from NiCr impregnation.

A broad absorption band between 3200 and 3800 $cm^{-1}$ appeared in almost all catalysts. These bands are attributed to O–H stretching vibrations arising from structural hydroxyl groups and adsorbed water molecules on the catalyst surface (Hahjiivanov, 2014). The persistence of hydroxyl groups indicates the retention of surface hydroxyl functionalities that can influence the hydrophilicity, adsorption behaviour, and surface reactivity of the catalysts. In aluminosilicate-based materials, hydroxyl groups associated with Si–OH–Al, silanol (Si–OH), and aluminol (Al–OH) environments can contribute to Brønsted acidity and provide sites for interactions with adsorbed reactant molecules. Such acidic hydroxyl sites are particularly important in acid-catalysed reactions relevant to biofuel conversion, where they facilitate reactant adsorption and subsequent chemical transformation (Liu and Bokhoven, 2024).

Upon impregnation with nickel and chromium, the FTIR spectra of NiCr/ATC and NiCr/BTC reveal noticeable changes in the hydroxyl region. The isolated hydroxyl bands generally decrease in intensity or shift to lower wavenumbers, indicating that surface hydroxyl groups participated in the coordination of $Ni^{2+}$ and $Cr^{3+}$ ions during impregnation. Such changes are characteristic of the formation of metal–oxygen–support (M–O–Si and M–O–Al) bonds and constitute strong evidence for successful metal anchoring (Hahjiivanov, 2014).

The H–O–H bending vibration observed in the range of 1615–1639 $cm^{-1}$ is consistently present in all the investigated materials and can be assigned to the deformation vibration of physically adsorbed molecular water. Similar bands near 1630 $cm^{-1}$ have been widely reported for silica and aluminosilicate materials and are attributed to water molecules adsorbed on the surface (Armandi et al., 2025; Ellerbrock et al., 2022). The persistence of this band after activation and metal impregnation indicates that the materials retain surface sites capable of interacting with water. Such behaviour is consistent with the presence of surface hydroxyl groups and siloxane/aluminosilicate oxygen functionalities, which can interact with water through hydrogen bonding. Consequently, the observed water adsorption provides evidence of the continued water affinity of the catalyst surfaces (Jo et al., 2022).

Weak absorption bands between 1270 and 1415 $cm^{-1}$ occur in nearly all the samples and are attributed to carbonate species, C–O stretching vibrations, or hydroxyl deformation modes (Stuart, 2004). These bands likely arise from trace inorganic carbonates or residual organic species remaining after synthesis. Their relatively low intensities indicate that thermal treatment effectively removed most organic constituents from the materials.

Generally, the FTIR results show a progressive evolution of the catalyst supports. Acid activation increases the abundance of surface hydroxyl groups, whereas alkaline treatment modifies the hydroxyl environment without destroying the aluminosilicate framework. Ni and Cr impregnation results in the interaction of the metal species with surface hydroxyl groups, leading to the formation of stable metal–oxygen–support bonds while preserving the structural integrity of the clay frameworks. These strong metal–support interactions are expected to improve metal dispersion, reduce metal leaching, inhibit sintering, and enhance catalyst durability and catalytic performance (Busca et al., 2024). When considered together with the XRF results, which confirmed the presence of Ni and Cr in the catalyst, and the XRD results, which showed changes in crystalline phases after impregnation, the FTIR results provide complementary evidence that metal loading occurred successfully.

The presence of hydroxyl groups, stronger carbonate-related bands, and the emergence of Ni–O/Cr–O vibrations in the NiCr-modified catalysts suggest improved metal–support interactions and more catalytically active sites. These are essential for aviation biofuel production reactions, including deoxygenation and catalytic cracking, which require efficient adsorption, oxygen removal, and hydrocarbon formation. Consequently, the NiCr-modified catalysts are expected to exhibit superior catalytic activity, selectivity, and durability compared with the unmodified catalysts.

Table 6: Interpretation of the Major FTIR Bands in ATC FTIR Spectrum

| **Wavenumber ($cm^{-1}$)** | **Assignment** | **Significance** |
|---|---|---|
| 3823 | Isolated structural O–H stretching | Indicates structural hydroxyl groups within the clay lattice. |
| 3652 | Al–OH/Si–OH stretching | Confirms preservation of structural hydroxyl groups after acid activation. |
| 3332 | Hydrogen-bonded O–H stretching | Surface hydroxyl groups and adsorbed water; contributes to hydrophilicity. |
| 3198 | Broad O–H stretching | Indicates abundant surface hydroxyl groups and enhanced adsorption capacity. |
| 2841 | Aliphatic C–H stretching | Minor residual organic matter. |
| 2703–2205 | Combination/overtone bands | Weak bands associated with structural vibrations or trace impurities. |
| 1944 | Combination/overtone of silicate vibrations | Indicates an ordered silicate framework. |
| 1626 | H–O–H bending vibration | Adsorbed water on the clay surface. |
| 1322 | C–O stretching or hydroxyl deformation | May reflect structural modification and increased surface functionality after acid treatment. |

Table 7: Interpretation of the Major FTIR Bands in BTC FTIR Spectrum

| **Wavenumber ($cm^{-1}$)** | **Probable Assignment** | **Significance** |
|---|---|---|
| 3806.18 | Isolated structural O–H stretching | Indicates structural hydroxyl groups remaining after alkaline treatment. |
| 2909.21 | Aliphatic C–H stretching | Suggests traces of residual organic matter or carbonaceous species. |
| 2671.89 | Hydrogen-bonded O–H stretching/combination band | Indicates retained surface hydroxyl groups and structural water. |
| 2057.70 | Combination/overtone vibration | Associated with the silicate framework. |
| 1937.38 | Combination/overtone of Si–O vibrations | Confirms preservation of the clay mineral structure. |
| 1618.38 | H–O–H bending vibration | Indicates physically adsorbed water on the clay surface. |
| 1404.20 | Carbonate or C–O stretching | May reflect minor carbonate or residual inorganic species. |
| 1274.56 | C–O stretching or hydroxyl deformation | Indicates surface functional groups and structural modification. |

Table 8: Interpretation of the Major FTIR Bands in NiCr/ATC FTIR Spectrum

| **Wavenumber ($cm^{-1}$)** | **Probable Assignment** | **Significance** |
|---|---|---|
| 3797.05 | Isolated Si–OH/Al–OH stretching | Surface hydroxyl groups; possible metal anchoring sites. |
| 3575.61 | Hydrogen-bonded O–H stretching | Structural hydroxyl groups retained after impregnation. |
| 3377.22 | Broad O–H stretching | Indicates abundant surface hydroxyl groups and adsorbed water. |
| 3226.17 | Hydrogen-bonded O–H stretching | Confirms hydroxylated catalyst surface. |
| 3025.81 | Weak C–H stretching | Trace residual organic species. |
| 2910.00 | Aliphatic C–H stretching | Minor carbonaceous residues. |
| 2670.78 | Hydrogen-bonded O–H/combination band | Indicates retained hydroxyl functionality. |
| 2527.68 | Combination vibration | Associated with the aluminosilicate framework. |
| 2461.50 | Overtone vibration | Structural silicate vibration. |
| 2119.66 | Si–O combination/overtone vibration | Indicates preservation of the silicate lattice. |
| 1915.48 | Combination band | Reflects an ordered aluminosilicate framework. |
| 1617.09 | H–O–H bending vibration | Adsorbed water on the catalyst surface. |
| 1397.03 | Carbonate or C–O stretching | Minor inorganic carbonate or residual impurities. |

Table 9: Interpretation of the Major FTIR Bands in NiCr/BTC FTIR Spectrum

| **Wavenumber ($cm^{-1}$)** | **Probable Assignment** | **Significance** |
|---|---|---|
| 3813.32 | Isolated Si–OH/Al–OH stretching | Surface hydroxyl groups serving as metal anchoring sites. |
| 3378.98 | Broad O–H stretching | Hydrogen-bonded hydroxyl groups and adsorbed water. |
| 3267.59 | O–H stretching | Confirms a hydroxyl-rich catalyst surface. |
| 3140.43 | Hydrogen-bonded O–H stretching | Indicates retained structural hydroxyl groups. |
| 3022.93 | Weak C–H stretching | Trace residual organic species. |
| 2864.44 | Aliphatic C–H stretching | Minor carbonaceous residues. |
| 2770.83 | Hydrogen-bonded O-H/combination band | Structural hydroxyl functionality. |
| 2618.41 | Combination vibration | Associated with the aluminosilicate framework. |
| 2452.56 | Overtone vibration | Structural silicate vibration. |
| 2237.13 | Combination band | Indicates preserved silicate lattice. |
| 2033.58 | Si–O combination/overtone vibration | Confirms an ordered silicate framework. |
| 1863.01 | Combination vibration | Supports structural stability of the support. |
| 1618.70 | H–O–H bending vibration | Adsorbed water on the catalyst surface. |
| 1385.29 | Carbonate or C–O stretching | Minor inorganic carbonate or residual impurities. |
| 849.94 | Symmetric Si–O–Si stretching | Confirms preservation of the silica framework. |
| 757.91 | Si–O–Al bending | Indicates retention of the aluminosilicate structure. |

### 3.4 BET Analysis

The surface area and pore volume of the synthesised catalysts were determined using the BET and DFT methods from nitrogen adsorption-desorption measurements at 77 K, respectively. The values and their interpretations are presented in Table 10. The textural properties of the synthesised catalysts, as determined from BET surface-area analysis and DFT pore-volume measurements, show that both the nature of the support and incorporation of NiCr species significantly influenced the porous characteristics of the materials. Among the unmodified supports, ATC exhibited the lowest specific surface area (167.728 $m^2/g$) and cumulative pore volume (0.055 $cm^3/g$), followed by BTC with 188.2 $m^2/g$ and 0.0586 $cm^3/g$, respectively. Another important observation is the effect of NiCr incorporation on the textural properties. For NiCr/ATC, the BET surface area increased from 167.728 to 252.7 $m^2/g$, accompanied by an increase in pore volume from 0.055 to 0.0865 $cm^3/g$. Similarly, in NiCr/BTC, the surface area increased from 188.2 to 314.0 $m^2/g$, with the pore volume increasing from 0.0586 to 0.0914 $cm^3/g$. These increases suggest that NiCr modification did not merely result in the deposition of metal species on the external surface of the support; rather, the synthesis procedure and subsequent thermal treatment appear to have induced structural reorganisation of the support, thereby modifying the accessibility of the pore network. Similar studies have demonstrated that metal incorporation can influence catalyst textural properties, while calcination can induce structural rearrangement, pore evolution and changes in the accessibility of supported metal species (Choi et al., 2026; Zhu et al., 2021).

**Table 10: The Textural Properties of the Synthesised Catalysts and Their Interpretations**

| Catalyst | BET surface area ($m^2/g$) | Pore volume ($cm^3/g$) | Textural interpretation |
|---|---|---|---|
| ATC | 167.728 | 0.0550 | Lowest surface development among the supports |
| BTC | 188.200 | 0.0586 | Slightly improved texture relative to ATC |
| NiCr/ATC | 252.700 | 0.0865 | NiCr incorporation improved textural properties |
| NiCr/BTC | 314.000 | 0.0914 | Strong enhancement of surface area and pore volume |

### 3.5 Catalyst Performance Evaluation

The performance of all the synthesised catalysts towards jet fuel-range hydrocarbons production were evaluated. The GC-FID results in Table 11 show that NiCr incorporation substantially altered both the overall liquid product yield and the carbon number distribution of the hydrocarbons. These changes correspond to differences in the textural properties of the catalysts, particularly BET surface area and pore volume (Table 10). However, the results indicate that surface area alone did not determine catalytic performance. Rather, catalytic behaviour appears to have been governed by the combined effects of surface area, pore architecture, active-site accessibility, support chemistry and the catalytic functions introduced by Ni and Cr. This interpretation aligns with reports that the performance of catalysts for vegetable-oil upgrading depends on the combined effect of surface area, pore structure, structural accessibility and acidity, with these properties also influencing the extent of primary cracking and subsequent secondary reactions and, consequently, the distribution of hydrocarbon products (Karilm et al., 2023; Das, 2025; Zhao et al., 2017).

The trend in the TLY of the catalysts is as follows: NiCr/BTC < ATC < BTC <NiCr/ATC (Table 11), while their BET surface areas are of the following order: ATC < BTC < NiCr/ATC < NiCr/BTC (Table 10). The result reveals that, in the case of ATC support, NiCr incorporation improved both the textural properties and TLY. In contrast, NiCr incorporation on BTC resulted in reduced TLY even as the textural properties improved. The corresponding increase in TLY with BET surface area and pore volume (ATC < BTC < NiCr/ATC) is consistent with the general principle that a highly developed porous surface can provide extensive contact between the feed and catalytic sites (Das, 2025). Nevertheless, the result of NiCr/BTC indicates that BET surface area should not be used as an isolated measure of catalyst performance. NiCr/BTC had a substantial surface area of 314 m2/g but produced only 64% TLY. Catalyst chemical properties such as acidity, can influence the extent of primary cracking and subsequent secondary reactions which determines the product distribution (Karilm et al., 2023; Das, 2025; Zhao et al. 2017). Hence, over cracking can result to production of more gaseous than liquid product. Thus, the chemical properties and accessibility of the active sites must have contributed significantly to the observed liquid yield.

The distinction between yield and selectivity is important in aviation-biofuel research. Research shows that when evaluating catalytic activity for jet-fuel production, evaluation must include both liquid-product yield and hydrocarbon carbon-range distribution because different catalysts can produce liquid products with substantially different hydrocarbon distributions (Nugraha et al., 2024; Asikin-Mijan et al., 2017; Nugraha et al., 2021). Table 11 shows that NiCr incorporation reduced jet-range selectivity with ATC catalysts (NiCr/ATC produced only 19.8% C8–C16 compared with 37.4% for ATC), but increased the same range with BTC catalysts (NiCr/BTC produced 20.1% C8-C16 compared to 15.4% for BTC). Similarly, C17-C19 selectivity increased from 8.4% to 24.5%, as C20+ selectivity decreased from 76.2% to 55.4% with NiCr incorporation on BTC. Whereas it produced a reverse effect in ATC catalysts. The C17-C19 hydrocarbons decreased from 15.2% to 2.2% as C20+ hydrocarbons increased from 47.1% to 78.0% with NiCr incorporation. Thus, introducing NiCr did not automatically improve aviation-range selectivity, notwithstanding increasing the BET surface area. It appears to have shifted the catalytic behaviour in the systems toward the production or retention of heavier hydrocarbons rather than maximizing the C8–C16 fraction. This implies that NiCr incorporation might have created an active site suitable for heavier hydrocarbon formation, possibly via oligomerization/condensation of olefin intermediates, cyclization or aromatization (Das, 2025). This indicates that the chemical nature of the newly introduced NiCr-containing active sites, rather than the increase in surface area, was more influential in determining carbon-range distribution. This behaviour aligns with literature showing that excessive or inappropriate acidity can promote over-cracking and secondary transformations rather than selectively producing aviation-range molecules. Catalysts intended for jet-fuel production generally require carefully controlled acidity and pore structure; excessively strong or abundant acid sites can promote uncontrolled cracking to lighter hydrocarbons (Karilm et al., 2023).

The substantial C20+ fractions observed for the two NiCr-containing catalysts warrant consideration of secondary reactions. In particular, NiCr/ATC generated 78% C20+ hydrocarbons despite having higher BET surface area than ATC. Such a distribution may indicate that primary cracking products underwent secondary transformations or that incomplete cracking of large molecules occurred. One possible pathway is oligomerization, in which smaller olefin intermediates react to form higher-molecular-weight hydrocarbons. However, Other pathways, including incomplete cleavage of triglyceride-derived chains, condensation, cyclization, aromatization and

insufficient secondary cracking, can also contribute to heavier hydrocarbons. Recent reviews of lipid catalytic pyrolysis identify cracking and aromatization as interconnected pathways that can modify carbon-chain length and product composition (Wang et al., 2022).

Table 4.25: The GC-FID analysis Result for deoxygenation and cracking of calabash seed oil

| Catalyst | %TLY | TPH (ppm) | C8-C16 (%) | C17-C19 (%) | C20+ (%) |
|---|---|---|---|---|---|
| ATC | 69 | 394.24 | 37.4 | 15.5 | 47.1 |
| BTC | 70 | 106.51 | 15.4 | 8.4 | 76.2 |
| RHS | 78 | 16.96 | 80.8 | 10.4 | 8.8 |
| NiCr/ATC | 71 | 55.6 | 19.8 | 2.2 | 78 |
| NiCr/BTC | 64 | 41.52 | 20.1 | 24.5 | 55.4 |

## 4.0. Conclusion

This study demonstrated the feasibility of developing multifunctional catalysts from locally sourced Ogbunike clay for the one-pot catalytic upgrading of calabash seed oil to hydrocarbon products. Acid and alkaline activation successfully modified the clay supports, while subsequent Ni–Cr impregnation introduced additional catalytic functionality without destroying the principal crystalline aluminosilicate framework. The XRF results confirmed the incorporation of Ni- and Cr-containing phases, whereas XRD and FTIR analyses indicated preservation of the support structure together with interactions between the metal species and surface hydroxyl/aluminosilicate functionalities. These characteristics suggest that the synthesized materials possess both acidic support sites and metal-associated functionalities capable of participating in the complex sequence of deoxygenation, cracking and secondary hydrocarbon-forming reactions required for vegetable-oil upgrading. The textural analysis further showed that Ni–Cr incorporation substantially increased the accessible surface area and pore volume of both activated clays.

The results of catalytic performance evaluation demonstrate that the effect of Ni–Cr modification was strongly dependent on the chemical and structural characteristics of the underlying support. The high C20+ fractions observed, particularly for NiCr/ATC, may reflect incomplete cracking and/or secondary reactions such as oligomerization, condensation, cyclization and aromatization.

In summary, the findings establish that Ogbunike clay is a promising low-cost support for multifunctional catalyst development and that Ni–Cr modification can substantially alter catalyst texture and hydrocarbon product distribution. Nevertheless, maximizing BET surface area should not be regarded as the sole objective in designing catalysts for aviation-range hydrocarbon production. Greater emphasis should be placed on controlling acidity, metal dispersion, pore architecture and the balance between primary cracking and secondary reactions. Further studies should therefore focus on optimizing Ni/Cr loading, catalyst acidity and reaction severity, as well as investigating catalyst regeneration, stability and recyclability. More detailed product characterization, including GC–MS and analysis of oxygenates, olefins, aromatics and individual hydrocarbon species, would also be valuable for establishing the reaction pathways responsible for the observed carbon-range distributions.

**Declaration of Generative AI and AI-assisted technologies in the writing process**

During the preparation of this work the authors used ChatGPT and Grammarly in sourcing for relevant materials and in refining syntax. After using these tools, the authors reviewed and edited the content as needed and take full responsibility for the content of the publication

**References**

Al-Fatesh A. S., Khatri J., Kumar R., Srivastava V. K., Osman A. I., Algarni T. S. et al. 2022. Role of Ca, Cr, Ga and Gd promotor over Ianthana-Zirconia-supported Ni Catalyst towards $H_2$- rich Syngas Production Through Dry Reforming of Methane. Energy Sci. Eng. 2022; 10:866-880. DOI: 10.1002/ese3.1063

Alherbawi, M., McKay, G., Mackey, H. R., and Al-Ansari, T. 2021. Jatropha curcas for jet biofuel production: Current status and future prospects. Renewable Sustainable Energy Reviews, 135, 110396.

Armandi M., Mohamed S. S. Y., Rombi E., Cutrufello M. G., Atzori L. and Onida B.2025. Heat of Water Adsorption on Large-pores Mesoporous Silica. J. Phys. Chem. C2025, 129, 14773-14780. https://doi.org/10.1021/acs/jpcs.5c02528

Asikin-Mijan, N., Lee, H., Juan, J., Noorsaadah, A., and Taufiq-Yap, Y. 2017. Catalytic deoxygenation of triglycerides to green diesel over modified CaO-based catalysts. RSC advances, 7(73), 46445-46460.

Bartholomew, C. H. (2001). Mechanisms of catalyst deactivation. Applied Catalysis A: General, 212, 17-60.

Busca G., Spennati E., Riani P. and Garbarino G. 2024. Properties, Industrial Application and Future Perspectives of Catalytic Materials Based on Nickel and Alumina: A Review. Catalyst 2024, 14, 552. https://doi.org/10.3390/catal14080552

Cheah, K. W., Yusup, S., Loy, A. C. M., How, B. S., Skoulou, V., and Taylor, M. J. 2022. Recent advances in the catalytic deoxygenation of plant oils and prototypical fatty acid models compounds: Catalysis, process, and kinetics. Molecular Catalysis, 523, 111469.

Choi S., Jeon Y., Kang D., Kim M., Ko C. 2026. Calcination-induced Pore Evolution in $TiO_2$ Supports Governing Ni Accessibility for Dry Methane Reforming. ChemistryOpen, 15:e202600011. https://doi.org/10.10002/open.202600011

Das P. 2025. A Review on the Catalytic Upgrading of Vegetable/Pyrolysis Bio-oil from Renewable Sources: Kinetic Studies and Environmental Impact Assessment. Catal. Sci. Technol. 2025, 15, 1406-1433. DOI: 10.1039/d4cy01475h

Ejiofor C.C., Nwabanne J. T., and Igbokwe P. K. 2026 Soxhlet Extraction and Characterization of Calabash Seed Oil as an Alternative Feedstock for Aviation Biofuel Production. UJCEE, (1), 1

Ellerbrock R., Stein M., and Schaller J. 2022. Comparing Amorphous Silica, Short-range-ordered Silicates and Silicic Acid Species by FTIR. Scientific Reports (2022)12:11708. https://doi.org/10.1038/s41598-022-15882-4

Gonzalez A.C., Weiss-Hortola E., Pham Q. N., and Minh D. P. 2025. Catalytic Methanation over Natural Clay-supported Nickel Catalysts. Molecules, 30, 2110. https://doi.org/10.3390/molecules30102110.

Gonzalez M. G., Nichio N. N., Moraweck B. and Martin G. 2000. Role of Chromium in the Stability of Ni/Al2O3 Catalysts for natural gas reforming. Mate. Letters 45 (2000) 15-18. https://doi.org/10.1016/S0167-577X(00)00065-3

Hadjiivanov, K. 2014. Identification and Characterization of Surface Hydroxyl groups by Infrared Spectroscopy. Advances in Catalysis (57) 99-314. http://dx.doi.org/10.1016/B978-0-12-800127-1.00002-3

He L., Ren Y., Yue B., Tsang S. C. E., and He H. 2021. Tuning Metal-Support Interactions on Ni/Al2O3 Catalysts to Improve Catalytic Activity and Stability for Dry Reforminf of Methane. Processes, 9, 706. https://doi.org/10.3390/pr9040706.

IATA 2026b. Fact sheet 2 – Sustainable Aviation fuel: Technical Certification. Retrieved 5th sept., 2026 from https://www.iata.org/contentassets/d13875e9ed784f75bac90f000760e998/saf-technical-certifications.pdf

IATA, 2026. Fact Sheet - sustainable aviation fuels. Retrieved 5th September, 2026 from: https://www.iata.org/en/iata-repository/pressroom/fact-sheets/fact-sheet-sustainable-aviation-fuels/

Jeon, K.-W., Shim, J.-O., Cho, J.-W., Jang, W.-J., Na, H.-S., Kim, H.-M., et al. 2019. Synthesis and characterization of Pt-, Pd-, and Ru-promoted Ni–Ce0. 6Zr0. 4O2 catalysts for efficient biodiesel production by deoxygenation of oleic acid. Fuel, 236, 928-933.

Jo H., Kim H and Yoon S. 2022. Synthesis and Characterisation of Mesoporous Aluminium Silicate and its Adsorption for Pb(II) ions and Methylene Blue in Aqueous Solution. Materials 2022, 15, 3562. https://doi.org/10.3390/ma15103562

Karilm I., Swai H., and Kivevele T. 2023. Bio-oil Upgrading Over ZSM-5 Catalyst: A Review of Catalyst Performance and Deactivation. Int. J. Energy Res. (2023), 4776962. https://doi.org/10.1155/2023/4776962

Khan, S., Lup, A. N. K., Qureshi, K. M., Abnisa, F., Daud, W. M. A. W., and Patah, M. F. A. 2019. A review on deoxygenation of triglycerides for jet fuel range hydrocarbons. Analytical Applied Pyrolysis, 140, 1-24.

Kim, T.-H., Lee, K., Kim, M. Y., Chang, Y. K., and Choi, M. 2018. Effects of fatty acid compositions on heavy oligomer formation and catalyst deactivation during deoxygenation of triglycerides. ACS Sustainable Chemistry Engineering, 6(12), 17168-17177.

Lim, M., Luckert, M. M., and Qiu, F. 2023. Economic opportunities and challenges in biojet production: A literature review and analysis. Biomass Bioenergy, 170, 106727.

Liu Q. and van Bokhoven J. A. 2024. Water Structure on Acidic Zeolites and Their Roles in Catalysis. Chem. Soc. Rev., 2014, 53, 3065-3095. DOI: 10.1039/d3cs00404j

Liu, Q., Zuo, H., Zhang, Q., Wang, T., and Ma, L. 2014. Hydrodeoxygenation of palm oil to hydrocarbon fuels over Ni/SAPO-11 catalysts. Chinese journal of catalysis, 35(5), 748-756.

Lokteva E. S. and Golubina E. V. 2019. Metal-Support Interactions in the Design of Heterogeneous Catalysts for Redox Processes. Pure Appl. Chem. 2019; 91(4): 609-631. https://doi.org/10.1515/pac-2018-0715

Mahene, W. L., Kivevele, T., and Machunda, R. 2023. The role of textural properties and surface chemistry of activated carbon support in catalytic deoxygenation of triglycerides into renewable diesel. Catalysis Communications, 106737.

McCabe R. W. and Adams J. M. 2013. Clay Minerals as Catalysts In Handbook of Clay Science (2nd ed. Pp 491-538). Elsevier. http://dx.org/10.1016/B978-0-08-098259-5.00019-6

Mofijur, M., Ahmed, S. F., Rony, Z. I., Khoo, K. S., Chowdhury, A. A., Kalam, M., et al. 2023. Screening of non-edible (second-generation) feedstocks for the production of sustainable aviation fuel. Fuel, 331, 125879.

Ng, K. S., Farooq, D., and Yang, A. 2021. Global biorenewable development strategies for sustainable aviation fuel production. Renewable Sustainable Energy Reviews, 150, 111502.

Nugraha, R. E., Prasetyoko, D., Asikin-Mijan, N., Bahruji, H., Suprapto, S., Taufiq-Yap, Y. H., et al. 2021. The effect of structure directing agents on micro/mesopore structures of aluminosilicates from Indonesian kaolin as deoxygenation catalysts. Microporous Mesoporous Materials, 315, 110917.

Nugraha, R. E., Prasetyoko, D., Nareswari, N. A., Aziz, A., Holilah, H., Bahruji, H., et al. 2024. Jet-fuel range hydrocarbon production from Reutealis trisperma oil over Al-MCM-41 derived from Indonesian Kaolin with different Si/Al ratio. Case Studies in Chemical Environmental Engineering, 10, 100877.

Patil, S. J., and Vaidya, P. D. 2018. On the production of bio-hydrogenated diesel over hydrotalcite-like supported palladium and ruthenium catalysts. Fuel Processing Technology, 169, 142-149.

Santillan-Jimenez, E., Morgan, T., Shoup, J., Harman-Ware, A. E., and Crocker, M. 2014. Catalytic deoxygenation of triglycerides and fatty acids to hydrocarbons over Ni–Al layered double hydroxide. Catalysis today, 237, 136-144.

Uzochukwu, J. S., Kanwulia, I. P., Tagbo, N. J., MC, J., Mary-Jane, E. C., and Nnayelum, O. C. 2025. Sustainable bio-aviation fuel production from biobased oil: a novel hydrogen-free biorefinery approach. UNIZIK Journal of Engineering Applied Sciences, 4(1), 1530-1554.

Walls, L. E., and Rios-Solis, L. 2020. Sustainable production of microbial isoprenoid derived advanced biojet fuels using different generation feedstocks: A review. Frontiers in Bioengineering Biotechnology, 8, 599560

Wang X., Wang H., Jin X., Wang F., and Shen B. 2022. Synthetic Strategies and Performance of Catalysts for Pyrolytic Production of Alternative Aviation Fuels Using Non-Edible Lipids: A Critical Review. Appl. Cata., 643, (2022), 118769. DOI: 10.1016/j.apcata.2022.118769.

Wang Y., Wu J., and Wang S. 2013. Hydrodeoxygenation of Bio-Oil Over Pt-based Supported Catalysta: Importance of Mesopores and Acidity of the Support to Compounds with different Oxygen Contents. RSC Advances, 2013, 3,12635. DOI:10.1039/c3ra41405a.

Wang, H., Lin, H., Feng, P., Han, X., and Zheng, Y. 2017. Integration of catalytic cracking and hydrotreating technology for triglyceride deoxygenation. Catalysis today, 291, 172-179.

Yamashita S., Yamamoto Y., Katayama M. and Inada Y. 2015. Kinetic Study on Solid-Phase Reduction of Silica-supported Nickel Oxide Species. Bull. Chem. Soc. Jpn. 2015, 88, 1629-1635. Doi: 10.1246/bcsj.20150243

Yang, J., Xin, Z., Corscadden, K., and Niu, H. 2019. An overview on performance characteristics of bio-jet fuels. Fuel, 237, 916-936.

Zhao X., Wei L., Cheng S., and Julson J. 2017 Review of Heterogeneous Catalysts for Catalytically Upgrading Vegetable Oils into Hydrocarbon Biofuels. Catalysis 2017, 7, 83; DOI:10.3390/catal1030083

Zhao, X., Sun, X., Cui, X., and Liu, D. 2019. Production of biojet fuels from biomass. In Sustainable Bioenergy (pp. 127-165): Elsevier.

Zhou L., Yang H., and Hu C. 2025. Catalytic deoxygenation of lipids for bio-jet fuel: Advances in catalyst design and reaction pathways. Catalysis 15, 518. https://doi.org/10.3390/catal15060518

Zhu H., Chen H., Zhang M., Liang C., and Duan L. 2024 Recent Advances in Promoting Dry Reforming of Methane Using Nickel Based Catalysts. Catal. Sci. Technol., 2024, 14, 1712-1729. DOI: 10.1039/d3cy01612a

Zhu S. Wang Y., Lu J., Lu H., He S., Song D., et al., 2021. Study of the Metal-Support Interaction and Electronic Effect Induced by Catalytic Performance of Glycerol Stem Reforming for Hydrogen Production: Nanomaterials, 11, 3149. https://doi.org/10.3390/nano11113149